



OPEN

## Annual and sub-seasonal dynamics of a rapidly eroding permafrost coastline along the Beaufort Sea in northern Alaska

Melissa K. Ward Jones<sup>1</sup>✉, Benjamin M. Jones<sup>1</sup>, Ingmar Nitze<sup>2</sup>, Matthias Gessner<sup>3</sup>, Guido Grosse<sup>2</sup>, Annett Bartsch<sup>4</sup> & Diana Bull<sup>5</sup>

Drew Point, an unlithified ice-rich permafrost coastline along the Alaskan Beaufort Sea, is among the most rapidly eroding Arctic coastlines, with an average erosion rate of 19 m/yr from 2007 to 2019. We use 16 high-resolution remote sensing datasets (satellite, airborne, and UAV imagery) to analyze erosion mechanisms (thermal abrasion and denudation) in relation to environmental forcings along a 1.5 km stretch of coastline during the 2018 and 2019 open water seasons. In a striking contrast, 2019 exhibited the highest mean erosion rate (34.5 m) within the 2007–2019 record, while 2018 had the second lowest (11.2 m). Block failure contributed to sub-seasonal erosion rates 6 to 21 times higher than thermal denudation, with staggered block fall timing, lag responses post-storm, and non-storm block collapse influencing overall erosion magnitude and timing. To quantify wind effects, we developed wind sums, a metric combining cumulative wind speed and directional data that can be used as a proxy for integrated storm intensity capable of incorporating lagged responses that correlated strongly with erosion at sub-seasonal and annual scales. Our findings emphasize the dominant role of wind during periods of open water and air temperature during the thaw season in driving permafrost coastline erosion dynamics, while highlighting the importance of spatiotemporally high-resolution datasets for understanding Arctic coastal change dynamics.

**Keywords** Drew Point, Alaska Beaufort Sea Coast, Coastal Erosion, Thermal abrasion, Thermal denudation, Block failure

Arctic coastlines represent the intersection between ocean and terrestrial permafrost systems. Approximately 34% of global coastlines are impacted by permafrost<sup>1</sup>. Of the coastlines impacted by permafrost, 35% are classified as lithified coasts that typically include rocky shorelines and fjords where erosion is primarily driven by freeze-thaw processes; the other 65% of coastlines are classified as unlithified deposits where erosion is driven by permafrost degradation<sup>2</sup>. Unlithified Arctic coasts are generally characterized by permafrost deposits that are actively eroding at variable rates<sup>1</sup> due to the temporal and spatial variability in terrestrial permafrost conditions, ground-ice content, sediment composition, ocean forcing, and hydrometeorological conditions<sup>1–3</sup>. Contemporary mean annual erosion rates at monitored locations that include both lithified and unlithified coasts vary between 0.1 m/year (Calypsostranda, Greenland Sea) to 17.2 m/year (Drew Point, Alaskan Beaufort Sea)<sup>4</sup> with average pan-arctic erosion rates projected to increase this century<sup>5</sup>. Coastal erosion processes are primarily restricted to the summer and fall seasons as sea ice presence and frozen conditions in winter causes these processes to become mostly dormant for eight to nine months of the year<sup>6</sup>. Changes to coastal systems and erosion rates affects the amounts of carbon and material exported to oceans<sup>5,7–10</sup> near-shore and terrestrial ecosystems<sup>11</sup> coastal morphologies<sup>2,6</sup> human subsistence lifestyles<sup>12</sup> and coastal infrastructure<sup>11,13</sup>.

The most rapidly eroding coasts in the Arctic are unlithified coastlines found in the Laptev, East Siberian and Beaufort Seas<sup>1,2,5</sup>. These coastlines are bonded by ice-rich permafrost, containing ~ 17–30% volumetric ground ice content or even more locally<sup>1</sup>. The dominant erosional processes of ice-rich permafrost coastlines are thermal denudation and thermal abrasion<sup>14–17</sup> resulting from their unique coastal cliff morphology<sup>16</sup>.

<sup>1</sup>Institute of Northern Engineering, University of Alaska Fairbanks, Fairbanks, USA. <sup>2</sup>Alfred Wegener Institute Helmholtz Centre for Polar and Marine Research, Potsdam, Germany. <sup>3</sup>Deutsches Zentrum für Luft- und Raumfahrt e.V. (DLR), Berlin, Germany. <sup>4</sup>b.geos GmbH, Korneuburg, Austria. <sup>5</sup>Sandia National Laboratories, Albuquerque, USA. ✉email: mkwardjones@alaska.edu

Thermal denudation refers to the slumping or subsidence of materials at the top of the bluff from ground ice melt under the influence of solar radiation, heat advection, and gravity<sup>16,17</sup>. Thermal abrasion (also referred to as thermo-mechanical erosion) occurs from the combined mechanical erosion from wave action (mechanical erosion) and thermal erosion from sea water that can also generate block failure<sup>14,15</sup>. Thermal abrasion generates the development of thermoerosional niches at the base of the coastal bluffs that recedes landward and causes toppling block failure and overhanging material to fall translationally<sup>17,18</sup>. To continue thermoerosional niche formation, any material in front of the bluff face, such as already fallen blocks that provide temporary protection from erosion, must be completely removed<sup>19</sup>.

Erosion of ice-rich permafrost bluffs occurs from a multitude of interconnected environmental parameters, including open water season (OWS) lengths, wave heights, ocean temperatures, meteorological conditions, permafrost temperatures, bluff height and bluff composition (sediments and ground ice content)<sup>2</sup>. Field observations, including the use of time lapse cameras, has shown that erosion is highly episodic with individual storm events able to contribute most of an annual total erosion amount in a given year<sup>19–21</sup>. Studies have shown that certain parameter changes, such as increased numbers of storms and longer OWSs, are coinciding with measured increased rates of erosion, and only a few studies have found significant correlations for mean erosion (particularly for abrasion processes) for ice-rich permafrost bluffs<sup>22–24</sup>. Challenges in studying Arctic coastal erosion processes include the remoteness of study locations and thus a lack of continuous observations and the focus of many studies on decadal observations<sup>12,25–31</sup> with few studies composed of annual<sup>21,24,32</sup> to sub-decadal observations<sup>22,23,33</sup>. Jones et al.<sup>21</sup> attributes the observed lack of correlations at Drew Point to (1) either insufficient resolutions or accuracies of parameters, (2) that erosion cannot be explained by annual dynamics but rather extreme weather events or long-term transient effects, or (3) that some parameters controlling erosion have not yet been considered in studies. Furthermore, remote sensing studies typically capture blufstop erosion as a response to erosional-niche development but do not directly measure the intricate processes driving niche formation.

One of the challenges of better understanding remote Arctic coastlines dynamics with environmental forcing factors is the lack of both high spatial and temporal resolution datasets. Our detailed study focuses on a subset of 1.5 km of coastline at Drew Point, located on the Alaskan Beaufort Sea Coast between Utqiagvik and Prudhoe Bay (Fig. 1). The studied coastline subset lies within the 9 km coastal segment initially investigated in Jones et al.<sup>21,27</sup> and we also provide an update to the 9 km erosion time series in Jones et al.<sup>21</sup> through to 2019. In addition, we provide a 16-image time series of the entire 2018 (5 timesteps) and 2019 (10 timesteps) OWSs using a combination of high-resolution remote sensing imagery from UAV surveys, airborne multispectral sensors (DLR MACS), and commercial satellites (Worldview, ©Maxar). The purpose of this study is to evaluate thermal abrasion and denudation erosion dynamics at annual and sub-seasonal scales in relation to environmental factors, including wind speed and direction, storms, air temperature, thawing degree day (TDD) sums, sea surface temperatures (SST), ground temperatures down to 1.2 m depth that includes the active layer and upper part of permafrost, and precipitation. We further identify statistically significant relationships between erosion and these environmental parameters across both sub-seasonal and annual timescales. By providing detailed insights into the drivers of erosion at high spatial and temporal resolution, this study improves our understanding of Arctic coastal dynamics of ice-rich unlithified coastlines and helps to inform predictions of future erosion of these coastlines in a rapidly changing climate.

### Study area

Drew Point lies in the zone of continuous permafrost within the Alaskan Coastal Plain along the Beaufort Sea Coast. It is located approximately halfway between Utqiagvik (formerly Barrow) and Prudhoe Bay (Fig. 1). Mean annual ground temperature is approximately  $-9^{\circ}\text{C}$ , measured at a depth of 20 m<sup>34</sup>. Permafrost in this region is ice-rich with pore and segregated ice accounting for 50 to 80% of the soil matrix and ice wedges contributing approximately 30% of the 80–90% total estimated volumetric ground ice content<sup>35</sup>. Ice wedges are typically 1 to 4 m wide and penetrate 3 to 5 m into the surface dissecting ice-rich Holocene-aged lacustrine silts with local peat accumulations. On average bluff heights are 4.4 m above mean water levels and eroded fine-grain sediment is typically transported away rather than accumulating at the base of the bluffs<sup>21</sup>. Erosional estimates of released total organic carbon into the Alaskan Beaufort Sea averaged 1,369 kg C m<sup>-1</sup> year<sup>-1</sup> between 2002 and 2018, doubling since the last half century<sup>36</sup>.

The orientation of the coastline section under study runs approximately east-west<sup>20</sup>. The most common wind direction at Drew Point, measured by a USGS automatic weather station (located at  $70^{\circ}51.872'\text{N}$ ;  $153^{\circ}54.405'\text{W}$ )<sup>37</sup> come from the east and northeast with a secondary maximum from the west. Surface winds coming from the west raise water levels and cause mixing of the stratified water column of varying temperatures<sup>20</sup>. Surface winds coming from the east drive down water levels away from the bluff face and lead to water cooling<sup>20</sup>.

Past studies at Drew Point have focused on coastal erosion and sea ice dynamics. Jones et al.<sup>27</sup> found decadal trends in increased rates of coastal erosion with mean annual rates increasing from 6.8 m/year to 8.7 m/yr to 13.6 m/yr for the time periods of 1955 to 1979, 1979 to 2002 and 2002 to 2007, respectively. Jones et al.<sup>21</sup> provided a decade of annual erosion amounts between 2007 and 2016 with a mean erosion rate of 17.2 m/yr for the whole period but found no significant correlation between erosion amounts and potential environmental divers. Barnhart et al.<sup>20</sup> used timelapse photography of erosion to calibrate a coastal erosion model to model erosion between 1979 and 2011 and found that the length of the OWS along with water temperature and exposure had the greatest control within the model for long-term coastal erosion rates. Both Overeem et al.<sup>38</sup> and Jones et al.<sup>21</sup> showed that the open water days have increased in length, up to a 1.54 days/yr. Barnhart et al.<sup>39</sup> found that the direction that has gained the greatest distance between the coast and ice edge in the summer is from the west (320 azimuth), therefore generating longer fetches and leading to increasing surge and waves height. Furthermore, the rapidity of erosion experienced at Drew Point makes it an ideal location to develop coastal

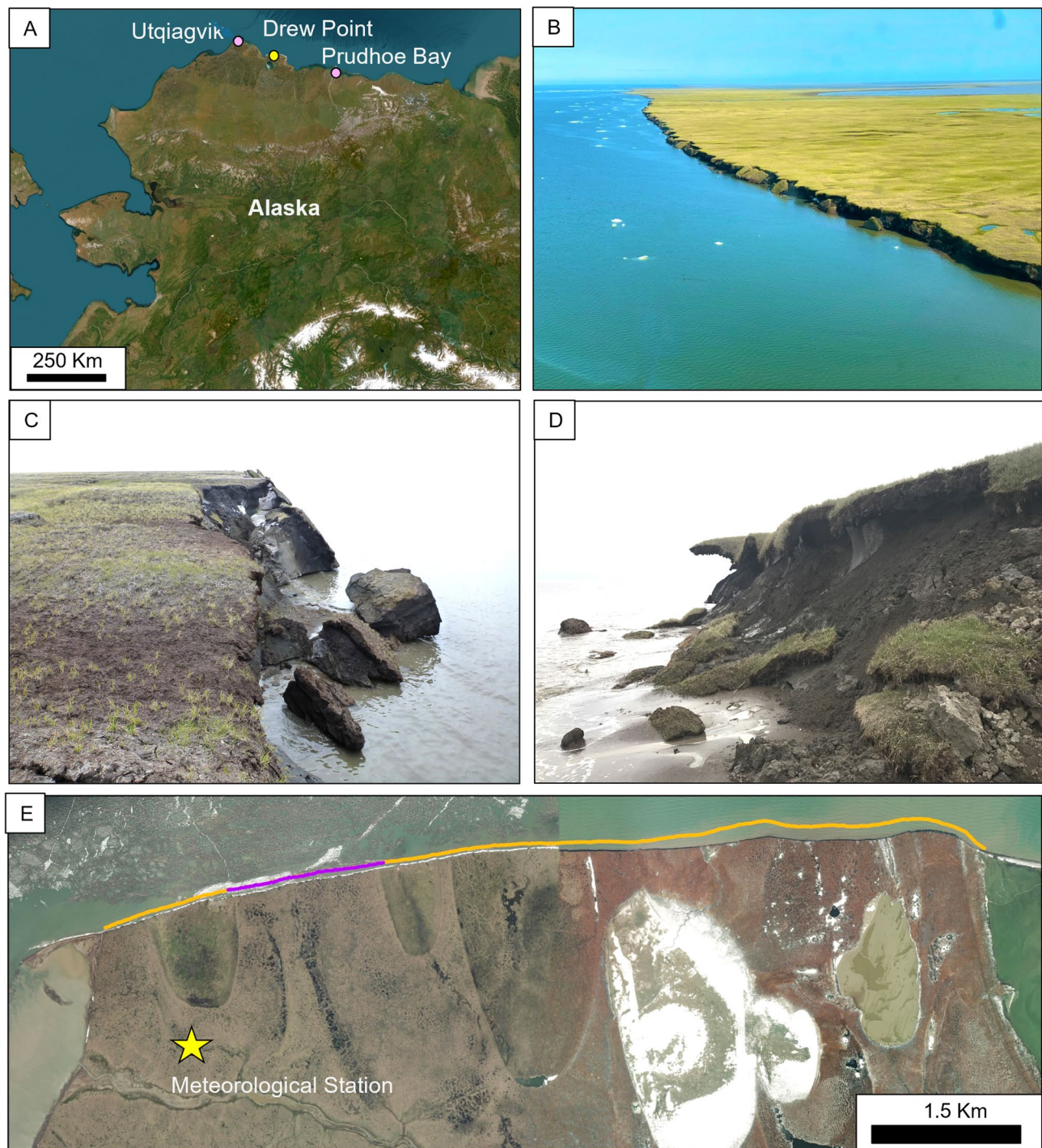


**Fig. 1.** Study area (A) shows the location of Drew Point along the Beaufort Sea Coast in Alaska, USA using ESRI basemap imagery; (B) a field image of the Drew Point Coastline from August 2021 showing collapsed blocks of ice-rich permafrost; (C) a field image of fallen blocks in various stages of dissolution; (D) material eroded by thermal denudation covering the bluff face and (E) the section of the Drew Point coastline under study. The orange line is the coastline from 14 April 2018 depicting the 9 km coastline for annual erosion measurements studied in Jones et al.<sup>21</sup>. The purple line represents the 1.5 km coastline under study for the sub-seasonal erosion dynamics presented here. ESRI basemap image from June and September 2023. Esri basemap imagery for (A) and (E) were accessed using ArcGIS Pro v. 2.7 (©ESRI); world imagery basemap sources: Esri, DigitalGlobe, GeoEye, i-cubed, USDA FSA, USGS, AEX, Getmapping, Aerogrid, IGN, IGP, swisstopo, and the GIS User Community. Photo in (B) was taken by M. Ward Jones. Photos in (C) and (D) were taken by B. Jones.

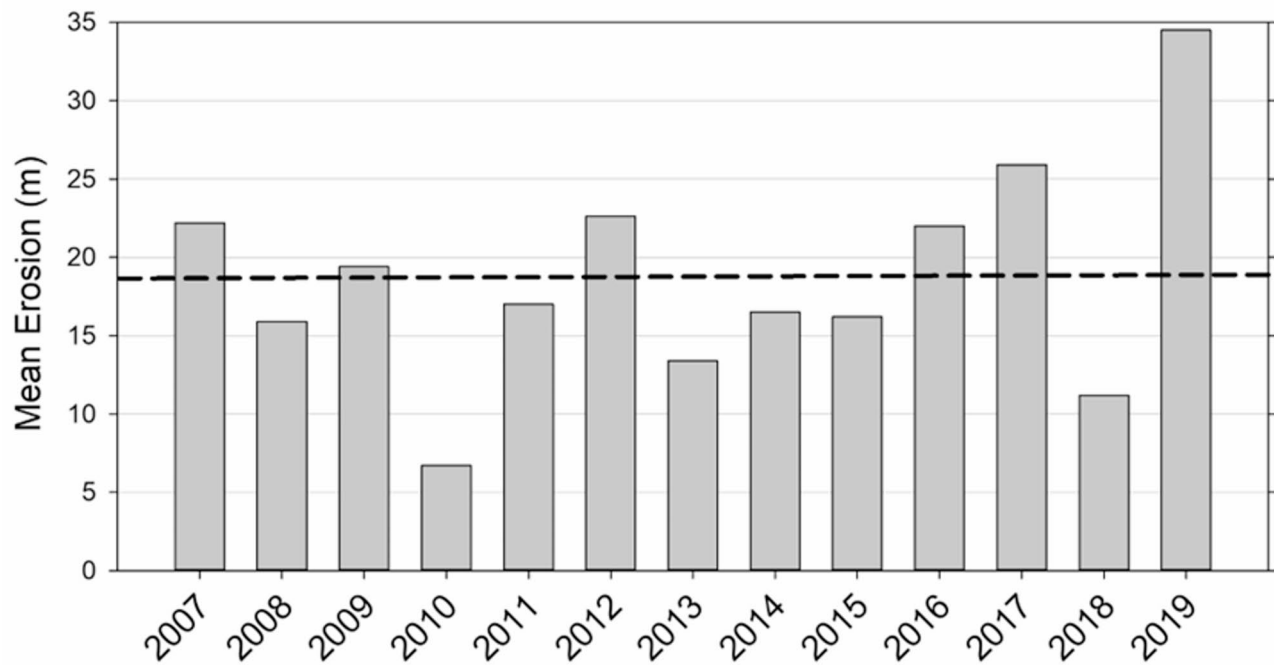
erosion models (e.g.<sup>20,40,41</sup>), and test new methods for measuring erosion such as the ICESat 2 satellite<sup>42</sup> and with Synthetic Aperture Radar (SAR) imaging<sup>43</sup>.

## Results and discussion

### Annual dynamics: erosion and environmental drivers

We updated annual erosion rates for the 9 km coastal segment of Drew Point, previously observed between 2007 and 2016<sup>21</sup>, through and including 2019. Between 2007 and 2019, annual erosion rates ranged from 6.7 m (2010) to 34.5 m (2019), with a total mean erosion of 18.7 m (Fig. 2). The 2019 erosion season recorded the highest erosion rate in the dataset (34.5 m), while the 2018 season (11.2 m) had the second lowest. Annual erosion rates were similar between the 9 km and 1.5 km sub-section of coastline in 2018 and 2019 (Figs. 1 and 2), indicating

## Annual Mean Erosion 2007 to 2019



## Sub-seasonal Mean Erosion 2018 and 2019

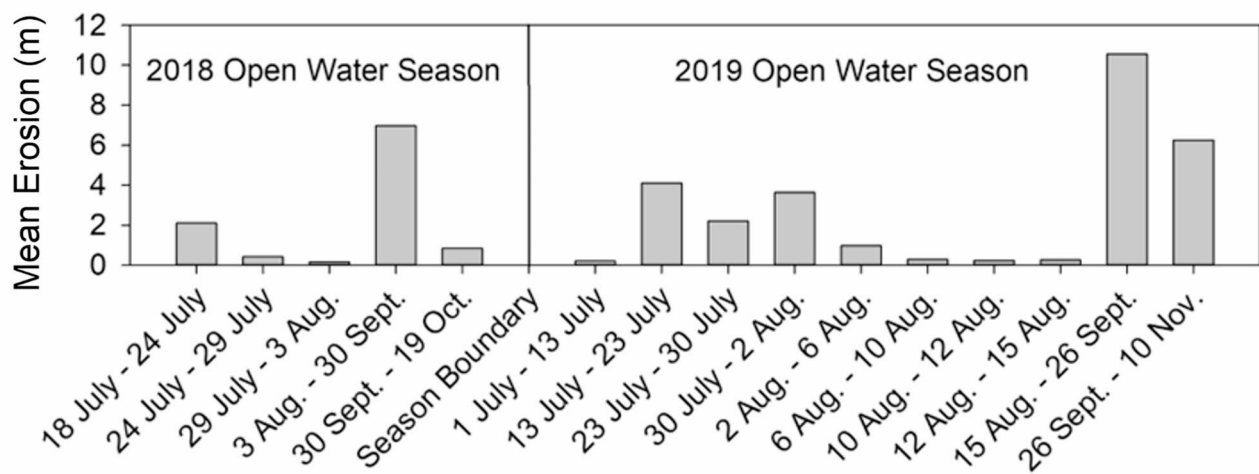


**Fig. 2.** Above, annual-scale erosion rates from 2007–2019 along a 9 km stretch of Drew Point (data from 2007–2016 is from Jones et al.<sup>21</sup>), AK. Below, sub-seasonal erosion rates for the 2018 and 2019 open water season for a 1.5 km subset of coast within the 9 km study area, see Fig. 1.

that the sub-section is representative of erosional patterns along the longer stretch of the Drew Point coastline. The annual erosion amount for the 1.5 km coastline was 10.5 m (2018) and 28.7 m (2019).

Comparing the annual data for environmental drivers of erosion (Table 1), 2019 had 39 more open water days compared to 2018 and mean OWS air temperature was 1.48 °C warmer, TDD sums was much higher (619 in 2019 vs. 273 in 2018), which led to warmer active layer and upper permafrost temperatures. The 2019 OWS also had more rain and warmer SST (4.3 °C in 2019 compared to 0.70 °C in 2018). One difference between both seasons is that when using the storm definition by Jones et al.<sup>21</sup> the 2018 OWS had one more storm event than 2019. Another notable feature of the 2018 season, which cannot be detected using coarser resolution satellite remote sensing products commonly used in annual erosion studies, is the persistent presence of permafrost blocks along the shore throughout the open water season. Higher-resolution airborne and UAV surveys allowed us to identify these blocks, and the dense temporal coverage provided valuable insights into their role in coastal erosion processes, as further discussed in the following section.

## Sub-seasonal processes during 2018 and 2019 open water seasons

### Erosion dynamics

Daily mean erosion rates (Fig. 3) varied between 0.04 m/day (30 Sept. – 19 Oct.) to 0.35 m/day (18 July to 24 July) during the 2018 OWS and varied between 0.02 m/day (1 July – 13 July) and 1.21 m/day (30 July – 2 Aug.) during the 2019 OWS. Assessing the magnitude of erosion at each timestep based on different processes, block failure contributed to 6 to 21 times higher erosion rates than thermal denudation during the entire study period. In the 2018 OWS, overall mean total block failure erosion varied up to 7.5 m during the 3 Aug. – 30 Sept timestep, and the only timestep with no block failure over the whole study period occurred during 29 July – 3 Aug. In 2019, the overall block failure rate was greater with mean total block failure erosion ranging between 4.0 m (12 Aug. to 15 Aug.) and 10.6 m (15 Aug. – 26 Sept.; Fig. 3).

The high spatial and temporal resolution of our approach allowed a classification of erosion for each transect in DSAS (see methods) based on erosion mechanism, either denudation or block failure (Fig. 3). Denudation was the dominant mechanism of erosion along 70% of transects but it contributes little to the overall total erosion amount (~ 0.2 m total). In contrast, thermal abrasion (block failure), representing episodic events at small sections of coastline, contributed significantly more erosion (rates up to 6 to 21 higher) compared to denudation. Our data shows that groups of blocks fall at different times but all within the same section of coastline (Fig. 4). Furthermore, block failure occurred along new sections of coastline until the majority of the coast was impacted by block failure to maintain coastline uniformity<sup>27</sup>. When timesteps consisted of a month or longer, we classified block failure for the majority of transects (over 90%) because while denudation would also be occurring, its contribution to total erosion is far less (3–16%) compared to the contribution from block failure.

We also assessed the number and total area of fallen blocks at the base of the bluff. The number of fallen blocks was greater during the 2018 OWS (98 to 122 counted blocks) than in the 2019 OWS (25 to 70 counted blocks). Total fallen block area varied between 1145 m<sup>2</sup> and 2954 m<sup>2</sup> in 2018 and 497 m<sup>2</sup> and 3413 m<sup>2</sup> in 2019. Within certain timesteps in 2018, such as 29 July – 3 Aug., and 3 Aug. – 30 Sept., there were similar block counts (98 and 104) but variable fallen block areas (1649 m<sup>2</sup> and 1145 m<sup>2</sup>), indicating that blocks broke down into smaller pieces as they dissolved without disappearing completely during the observed timeframe. Barnhart et al.<sup>20</sup> reported blocks needing 10 days to completely degrade. Jones et al.<sup>21</sup> showed timelapse imagery with blocks degrading in about two weeks. Previously fallen blocks have been considered negligible in overall erosion dynamics at Drew Point<sup>20,40</sup> but the 2018 OWS shows that their presence can have an overall impact on erosion rates. Fallen blocks serve as temporary bluff protection and must be completely removed for further bluff abrasion to occur<sup>19</sup>. The 2018 season had the lowest SST of any season between 2007 and 2019 (this study and Jones et al.<sup>21</sup>), which likely contributed to decreased rates of block dissolution.

Fallen blocks in front of the bluff face protected between 29 and 51% of the coast in 2018 and 9–48% of the coast in 2019. Erosion rates within protected sections of the coast ranged from 0.03 m/day (30 Sept. – 19 Oct.) to 0.09 m/day (3 Aug. to 30 Sept.) in 2018 and between 0.03 m/day (6 Aug. – 10 Aug.) and 0.54 m/day (30 July – 2 Aug.) in 2019. Erosion in protected areas was primarily by denudation except for a few instances where the edge of a newly fallen block landed beside a previously fallen one (see Fig. 4 as example). Exposed sections of coastlines had higher overall erosion, mean daily erosion ranged between 0.04 m/day (29 July – 3 Aug.) and 0.13 m/day (24 July – 29 July and 3 Aug. to 30 Sept.) and in 2019 varied between 0.4 m/day (23 July – 30 July) and 1.56 m/day (2 Aug. – 6 Aug.).

	2018	2019
OWS Total Duration (days)	93	132
OWS Mean Air Temperature (°C)	5.10	6.58
OWS TDD	273	619
OWS Mean/Max Active Layer Temperature (°C)	1.71/4.83	2.71/5.12
OWS Mean/Max Upper Permafrost Temperature (°C)	-1.66/-1.12	-1.43/-0.80
OWS Total Precipitation at Utqiagvik (mm)	19.78	60.59
OWS Total Storm Count	9	8
OWS Mean Sea Surface Temperature (°C)	0.70	4.3

**Table 1.** Comparing environmental factors for the duration of the 2018 and 2019 open water season (OWS).

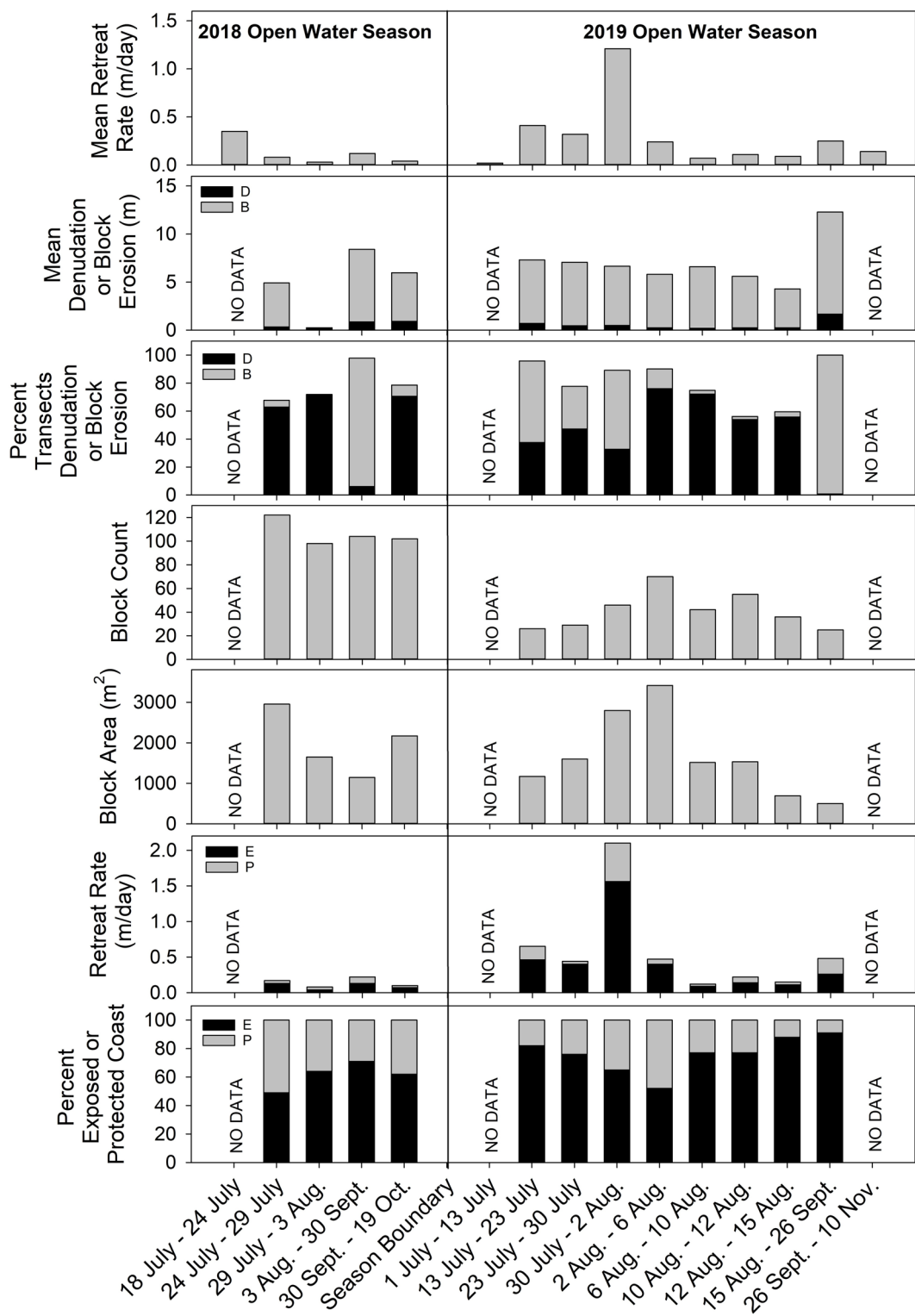


**Fig. 3.** Sub-seasonal erosion dynamics during the 2018 and 2019 open water seasons. From top to bottom the graphs show the following: mean retreat rate in m/day, mean denudation or block erosion, percent transects that recorded either denudation or block erosion, block count, block area, retreat rate (m/day) of both exposed and protected segments of coastline and the total percentage of exposed or protected coastline.



**Fig. 4.** Three consecutive timesteps of UAV imagery (10, 12 and 15 August) showing the same sub-section of coastline during the 2019 open water season. The timesteps show a section of coast where block failures occurred in three successive timesteps. The failures occurred from an east to west direction. These failures likely represent post storm lag of block failure from a storm that occurred within the 30 July to 2 August timestep.

#### *Sub-seasonal environmental drivers and erosion responses*

We assessed potential environmental drivers (mean air temperature, TDD sums, mean active layer temperature, mean permafrost temperature, hourly precipitation at Utqiāġvik, number of storms, wind dynamics, and mean SST) of erosion for each timestep at Drew Point (Fig. 6). Mean air temperature varied between  $-2.8\text{ }^{\circ}\text{C}$  and  $10.8\text{ }^{\circ}\text{C}$  throughout the study period. TDD sums also varied and because TDD sums are calculated based on the number of days of the timestep, timesteps with longer duration generally had higher TDD sums, but not because those time periods were necessarily warmer (as denoted by mean air temperature). Mean active layer temperature (between 5 cm and 30 cm depth) dynamics mirrored mean air temperature except when the ground was thawing in the earliest timesteps for each OWS. Mean permafrost temperatures (between 45 cm and 120 cm depths) gradually warmed during each OWS. In 2018, mean SST only went above  $0\text{ }^{\circ}\text{C}$  during one timestep (3 August to 30 September), whereas in 2019, mean SST was only below  $0\text{ }^{\circ}\text{C}$  during one timestep (1 July to 13 July) and then ranged between  $5.7\text{ }^{\circ}\text{C}$  and  $8.1\text{ }^{\circ}\text{C}$  for subsequent timesteps. Precipitation measured at Utqiāġvik was highly variable throughout the study period ranging between 9 mm and 422 mm. Storms occurred mostly in the late summer and fall periods. Storms were classified as westerly ( $240\text{ }^{\circ}$  to  $360\text{ }^{\circ}$ ) and easterly ( $0\text{ }^{\circ}$  to  $90\text{ }^{\circ}$ ) to provide additional insight into analysis.

We conducted linear regression analysis between environmental parameters and our sub-seasonal erosion rates (including only sub-seasonal block failure and denudation erosion, Fig. 7). We found that TDD sums and the number of storms yielded the highest  $R^2$  values at sub-seasonal timescales. TDD sums had  $R^2$  values of 0.476, 0.715 and 0.963 for sub-seasonal total, block failure, and denudation erosion, respectively. Denudation erosion is primarily driven by thawing processes, therefore its high correlation with TDD sums is not surprising. The high correlation with block failure erosion may be due to the influence of air temperature and accompanied radiative heating on ocean water at the bluff edge, a parameter that has been shown to be potentially a primary driver

of erosion through modelling<sup>20</sup>. The number of storms correlated highest for total sub-seasonal erosion ( $R^2 = 0.539$ ), followed by denudation ( $R^2 = 0.457$ ) and then block failure erosion ( $R^2 = 0.161$ ). The impact of storms is primarily driven by wind strength and direction, however using storm counts is a limiting parameter because a storms' impact on erosion can continue after the event is over (lag responses of erosion<sup>26</sup>), which was observed in August 2019 (Fig. 4). To gain a deeper insight into the potential role of wind as a driver of erosion, each timestep and OWS was divided into a wind rose diagram (Fig. 5).

Wind direction fluctuates highly during each timestep. Overall, the 2018 OWS experienced primarily easterly winds and the 2019 OWS experienced more easterly winds, followed by westerly winds, but westerly winds were also accompanied by greater more frequent wind speeds, particularly for speeds above 10 m/s. Comparing wind speed and direction with sub-seasonal erosion dynamics, overall westerly winds correspond with periods of increased mean daily erosion. The three timesteps with the highest mean daily erosion and corresponding dominant wind directions are 30 July to 2 August 2019 (1.2 m/day, westerly winds), 13 July to 23 July 2019 (0.4 m/day, westerly with northwest to easterly variability) and 18 July to 24 July 2018 (0.4 m/day, westerly). The 2018 OWS generally experienced more frequent easterly winds with some short time intervals of westerly winds with high (> 10 m/s) wind speeds. The timing of these westerly wind events corresponds to higher rates of erosion, such as the 3 August to 30 September timestep (7.0 m of mean total erosion). The only timestep with no block erosion (29 July to 3 August 2019) experienced only easterly winds. Furthermore, easterly winds generally correspond with timesteps with decreasing block area, however the 2018 OWS consistently had a high presence of blocks and primarily easterly winds, therefore other factors such as SST which was low (average 0.7 °C for the whole OWS) likely also contribute to processes that slow down the rate of blocks dissolving. These observations suggest that it is important to parse out erosional processes relative to environmental forcing factors to improve predictions.

Wind controls many processes that can drive erosion: water levels (at Drew Point, westerly winds increase water levels and easterly winds decrease water levels), wave dynamics including wave height and fetch, as well as transporting weather fronts affecting air temperatures. Assessing wind-driven environmental parameters and erosion dynamics during our study period at Drew Point, we contribute the following observations:

- (1) Our findings show that westerly and northwesterly wind events are more effective earlier in the erosion season when air, ocean, and permafrost temperatures are warmer, making them primary drivers of erosional niche development.
- (2) Northeasterly to easterly winds play a critical role in dissolving permafrost blocks, removing the temporary bluff protection and setting the stage for niche development when water levels are sufficient. This process increases the impact of subsequent westerly storms, which drive further erosion through niche development.
- (3) Lower-intensity winds can still drive erosion outside of storm events. In 2019, while storms-initiated niche development and widespread block failure, final block collapse occurred post-storm, with neighboring blocks falling at different times (Fig. 4). These dynamics create lag responses in the timing of erosion, complicating correlations between erosional drivers and erosion rates.

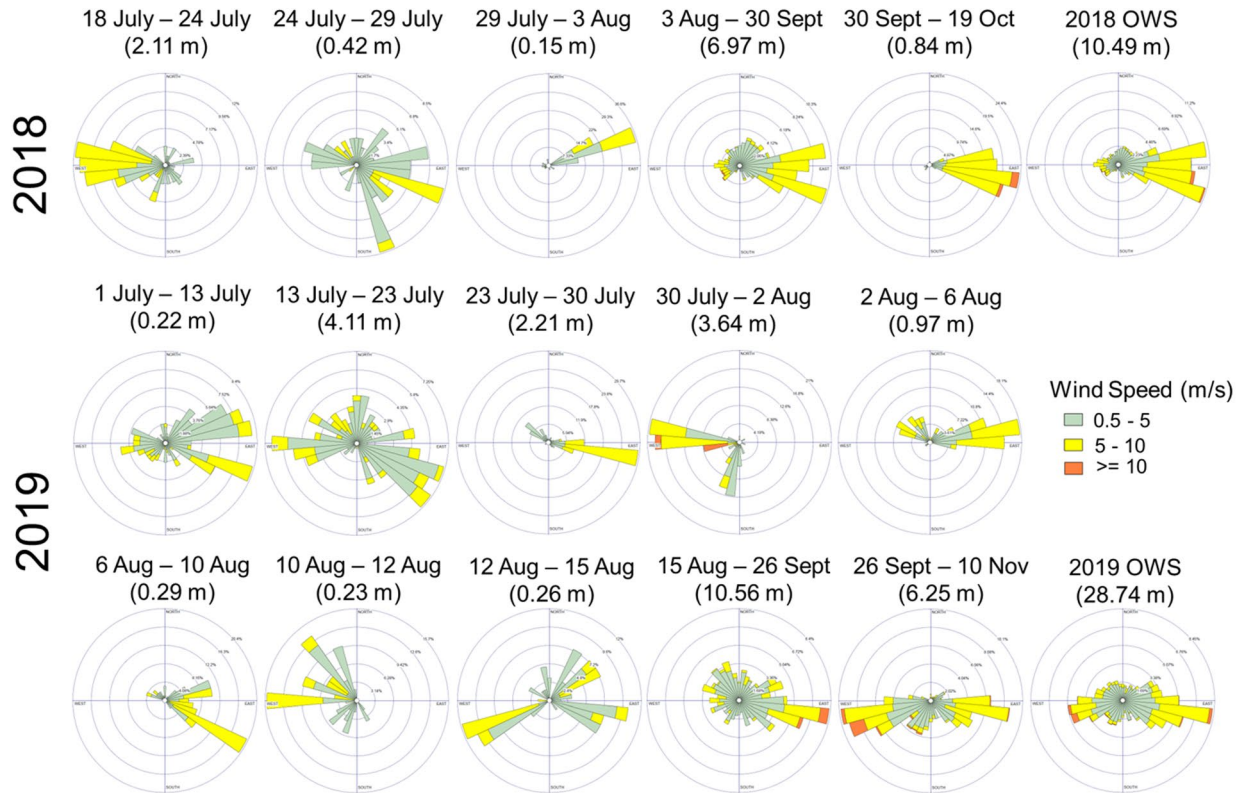
To improve our understanding and to find correlations between environmental drivers of erosion we developed a new environmental metric called wind sums. Wind sums are calculated the same way as TDD sums, so that hourly mean windspeeds are summed together for the period of interest. These periods can be sub-seasonal or for an entire open water season. We also classify wind sums as either total wind sums (all directions are included in the calculation) or directional wind sums (only windspeeds from directions of interest are included in the calculation, other directions are excluded). We believe wind sums are effective for correlating with erosion because they can account for periods of storms, as elevated winds in storms generate higher wind sums as well as accounting for lag effects of block failure since winds after storms can finalize the wave action needed for block failure to occur. Our linear regression  $R^2$  for total wind sums was 0.533 (total sub-seasonal), 0.285 (block), and 0.693 (denudation). For directional wind sums, westerly to north westerly wind sums (240 ° to 90 °) yielded  $R^2$  values of 0.692 and 0.534 for total sub-seasonal and block erosion. Directional wind sums under Jones et al.<sup>21</sup>'s storm definition (240 ° to 90 °) yielded  $R^2$  values of 0.591 and 0.261 for total sub-seasonal and block erosion. Denudation erosion regressions using directional wind sums (which uses a subset of the wind data based on direction) did not satisfy normality or constant variances tests and were therefore excluded.

We also conducted multiple linear regression to further assess how environmental parameters may work together to contribute to total sub-seasonal erosion amounts. We found that the combination with the highest  $R^2$  (0.870) was TDD sums, SST, and 240 ° to 360 ° directional wind sums.  $R^2$  values decreased to 0.829 and 0.801, respectively, when 240 ° to 90 ° directional wind sums or total wind sums (log) were used instead. This variable combination represents multiple processes: TDD sums and wind sums primarily controlling coastal erosion mechanisms and SST contributing to block dissolution.

### Reassessing annual dynamics with sub-seasonal insights

In addition to conducting linear regression analysis for 2018 and 2019 sub-seasonal erosion rates, we also considered regression for annual rates, adding three additional OWSs and building on the initial analysis conducted by Jones et al.<sup>21</sup>. Like Jones et al.<sup>21</sup> we find correlations for annual retreat to be negligible for all environmental parameters (e.g. Figure 7 shows  $R^2$  values of 0.00659 and 0.0160 for TDD sums and number of storms, respectively) except for wind sums. Total wind sums had an  $R^2$  of 0.588 and directional wind sums were 0.308 for westerly to north westerly winds (240 ° to 90 °) and 0.0686 for wind directions within Jones et al.<sup>21</sup> storm definition (240 ° to 90 °).

## Sub-seasonal Wind Dynamics



## Annual Wind Dynamics

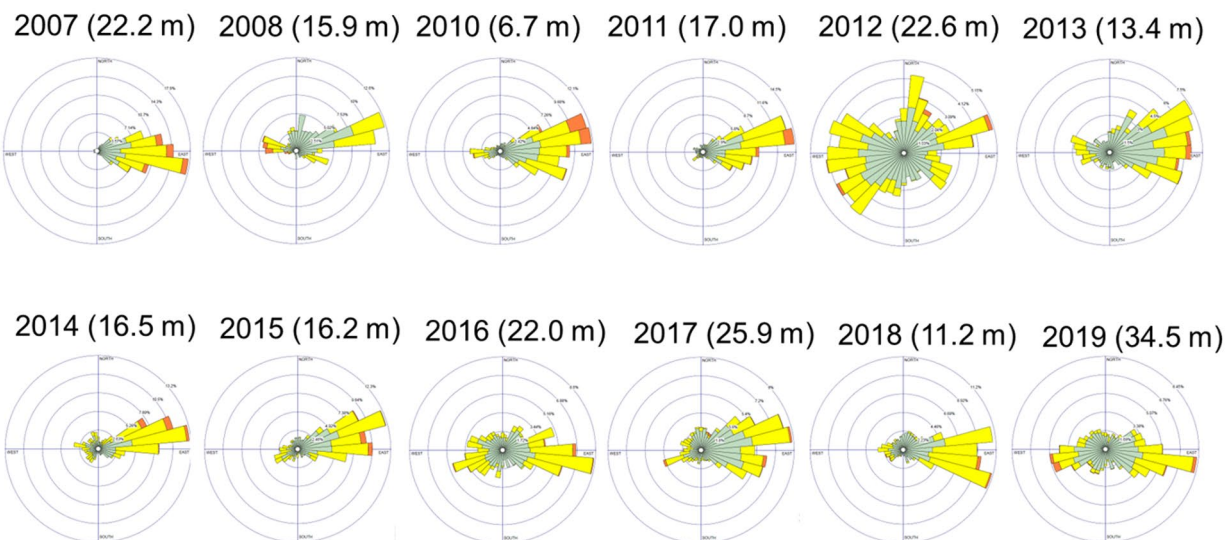


**Fig. 5.** Above: sub-seasonal wind rose diagrams for each 2018 and 2019 timesteps as well as for the whole open water season (OWS) for the 1.5 km section of coastline under study. Below: annual wind rose diagrams for the 9 km stretch of coastline in Jones et al.<sup>21</sup>. Note that 2009 is not included due to lack of data from a faulty sensor.

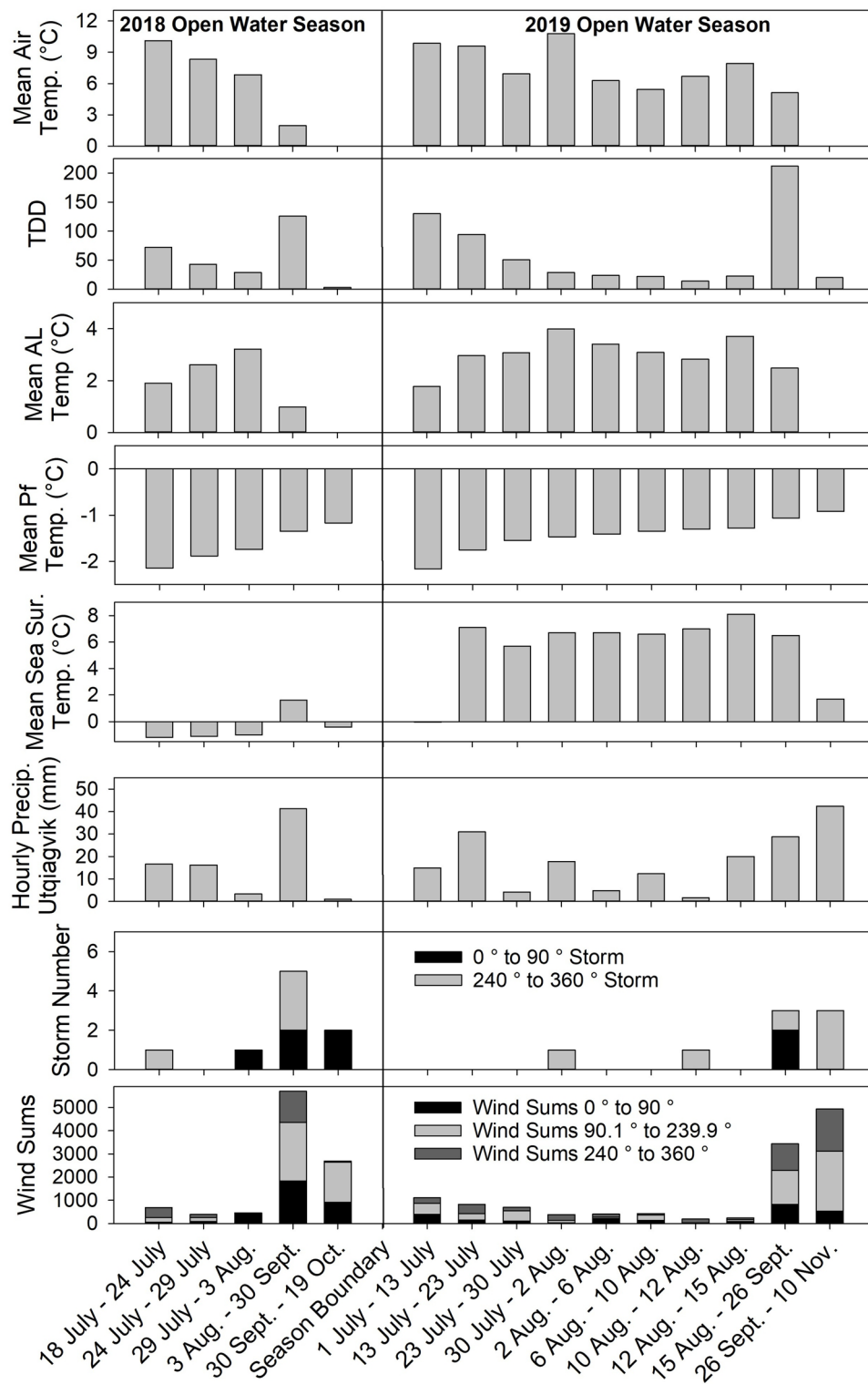


**Fig. 6.** Environmental parameters during the 2018 and 2019 open water seasons, all measured at Drew Point except for precipitation which was measured in Utqiagvik. Top to bottom graphs show the following: mean air temperature, thawing degree day (TDD) sums, mean active layer temperature (measured at 5 cm, 10 cm, 15 cm, 20 cm and 30 cm depths), mean permafrost temperature (measured at 45 cm, 70 cm 95 cm and 120 cm depths), mean sea surface temperature, storm number (storms defined by<sup>21</sup>) and wind sums.

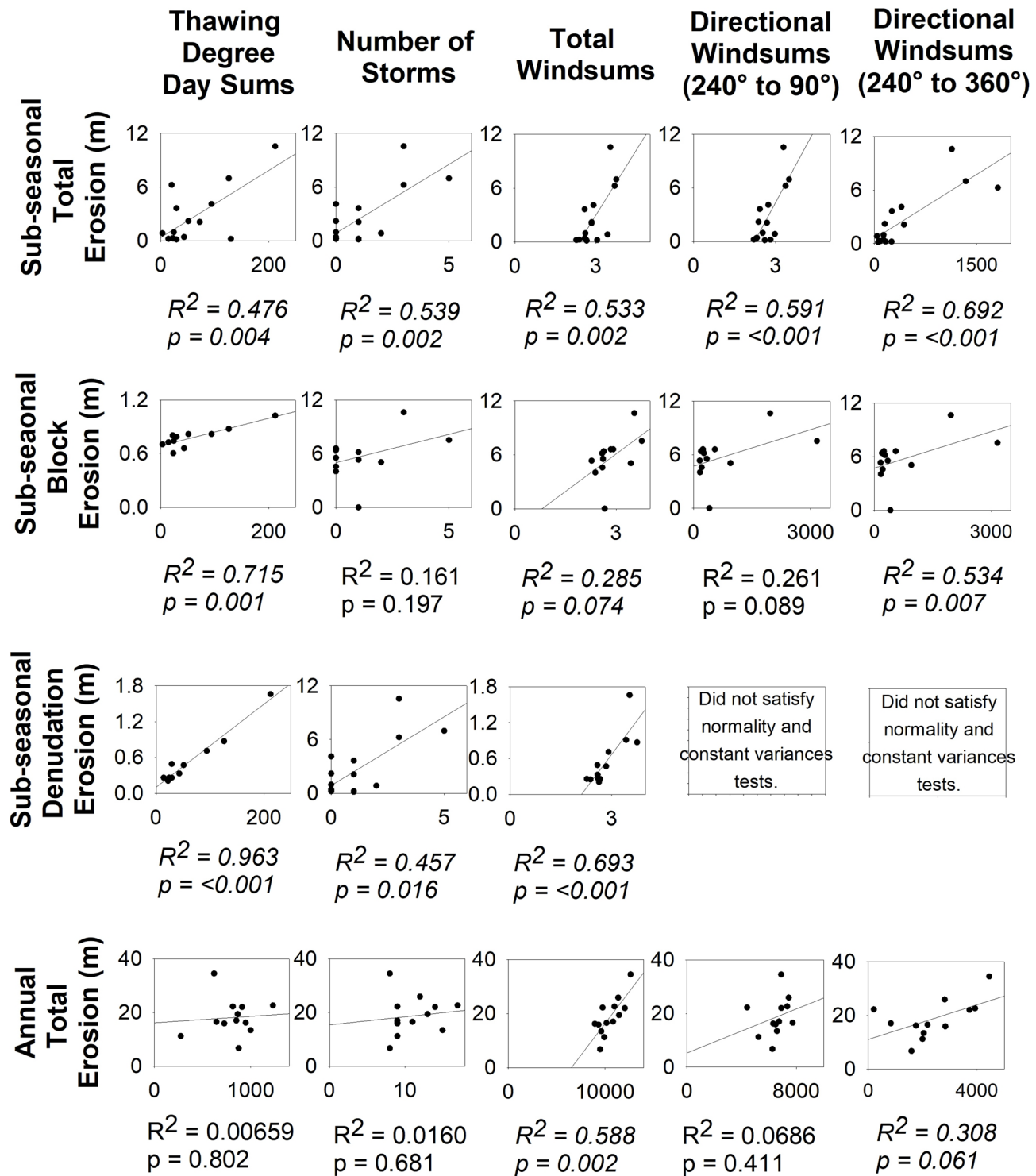


**Fig. 7.** Linear regression outputs between sub-seasonal total, block, denudation as well as annual erosion and thawing degree day sums, number of storms, total wind sums and direction wind sums (240° to 90°, and 240° to 360°).

Whereas our sub-seasonal analysis of the 2018 and 2019 OWS found the likely environmental parameters responsible for erosion rates for those seasons, these specific parameters may not be universal for each season. We found that the 2018 season had limited erosion due to the constant presence of blocks in front of the bluff face. Block dissolution was likely limited by the colder air and ocean temperatures and persistent easterly to northeasterly winds (Table 1). The 2019 OWS showed how effective westerly winds are in eroding the coast and that block fall events can lag in time after the storm.

Reviewing annual wind rose diagrams and erosion rates (Fig. 5) shows that the 2019 OWS had the most frequent and strongest westerly wind events and is accompanied by the highest erosion rate (34.5 m) in our record. The 2018 OWS had less erosion (11.2 m) compared to other years also dominated by easterly winds: 2007 (22.2 m) and 2011 (17 m). A timestep in 2018 (3 Aug. to 30 Sept.) with less frequent westerly events but accompanied by higher wind speeds and a higher rate of daily erosion supports the idea that easterly winds can make subsequent westerly wind events more effective for erosion<sup>27</sup>. Our sub-seasonal observations show this is likely due to easterly winds facilitating faster dissolving of blocks and thus enhancing exposing the coast for westerly winds to be more effective. 2007 and 2011 were also accompanied by higher SSTs (3.5 ° and 2.3 °), compared to 2018 (0.70 °C), demonstrating that certain environmental parameters must be coupled to be effective in driving increased rates of erosion. This could be why total wind sums are the only environmental parameter to our knowledge that provides the highest  $R^2$  values for annual erosion rates using linear regression at Drew Point, as this parameter is representative of integrating multiple environmental factors: water levels, wave heights, changing weather fronts and storm events. When combining multiple parameters using multiple linear regression, we find that using the same combination of variables (SST, TDD sums, and winds sums) for sub-seasonal erosion can be successfully applied to annual rates. The highest  $R^2$  obtained was 0.702 when total wind sums were used. When directional wind sums were used,  $R^2$  values decreased to 0.699 (240 ° to 360 °) and 0.554 (240 ° to 360 °), respectively. Our results align with those found by Gibbs et al.<sup>24</sup> who obtained a multiple linear regression  $R^2$  of 0.92 for wave power (derived by modelling), normalized cumulative positive degree days (similar to our TDD sums), and normalized cumulative degree day positive sea surface temperatures for 17 timesteps of coastal erosion at Barter Island, also on the Beaufort Sea Coast between 1979 and 2019. Our results show that wind metrics, specifically wind sums, can be used as an indicator of wave action to achieve high  $R^2$  values in the absence of using data from wave buoys or models.

Other environmental parameters contribute to erosion rates that were not considered in this study. These include wave dynamics (such as height and fetch), water level dynamics, and distance to sea ice<sup>20,24,38</sup>. Another parameter is the presence of saline permafrost and cryopegs (stratigraphic layers that are below 0 °C but remain unfrozen due to high salt contents)<sup>21</sup>. The presence of saline permafrost and the effects of its warming have likely factored into documented increases in rates of arctic coastal erosion. Porewater salinity measured along bluffs at Drew Point with varying heights above mean sea level all show the presence of saline permafrost ~ 2 m above and below beach level, which means that saline permafrost occurs in the zone where thermo-mechanical erosion niches develop<sup>36</sup>. We hypothesize that the warming of saline permafrost has likely contributed to an increase in landscape change rates with one of the factors being an increase in the rate of niche formation and block failure and ultimately in the rate at which unlithified arctic coasts erode.

Overall, our sub-seasonal observation provided the following observations that can aid in the interpretation of annual erosion rates:

- (1) It is important to parse out erosional processes relative to environmental forcing factors to improve predictions.
- (2) Block failure often occurs at different times along the same section of coast, and these block fall dynamics contribute to lag responses post-storm and thus what can be measured from remote sensing images depends on imagery resolution and timing.
- (3) The presence of toppled blocks impacts overall erosion rates by providing temporary protection and must be considered to accurately interpret erosion dynamics and to make projections.
- (4) Block failure can still occur during non-storm events, particularly in driving the final amount of erosion for niche dimensions needed for failure to occur.

## Methods

### Remote sensing data collection and delineation of bluff edge and blocks

Sixteen timesteps spanning the entire 2018 and 2019 open water seasons were used from various imagery sources including higher resolution satellite imagery, airborne multispectral imagery and UAV surveys (Table 2). Satellite imagery used included Worldview 1 imagery (50 cm pixel resolution, ©Maxar) for 14 April 2018, and Worldview 2 panchromatic imagery (46 cm pixel resolution, ©Maxar) for 5 April 2019, 26 September 2019, and 3 April 2020. The airborne multispectral imagery was collected using a Modular Aerial Camera System (MACS-Polar) during the Polar-6 airborne operations during the ThawTrend-Air campaign with timesteps collected on 13, 23 and 30 July 2019. UAV surveys were collected in 2018 on 24 July, 29 July, 3 August and 30 September and in 2019 on 2 August, 6 August, 10 August, 12 August and 15 August.

MACS-Polar is an airborne multispectral optical measurement system. It was developed by the DLR Institute of Optical Sensor Systems for scientific purposes<sup>44</sup>. The design allows for flexible adaptation to unusual carriers, environment and measurement tasks. Geometric and radiometric constellations as well as functional capabilities can be implemented and tested directly on the system. To acquire permafrost images over Alaska, the sensor head was placed in the Polar-6 research aircraft belly payload bay.

The sensor configuration consisted of two slightly left-right tilted RGB cameras with a 90 mm lens (RGB wavelength 400–680 nm) and one nadir looking near-infrared camera with a 50 mm lens (wavelength NIR, 700–950 nm). The nadir camera images cover approximately the same ground swath as both stitched RGB images. For the RGB cameras a ground sampling distance of 9 cm from an altitude of 1,000 m above ground level was achieved. All sensors and their optics were calibrated geometrically and for radiometric correction. Images

Sensor and Image Type	Date Acquired	Pixel Resolution (cm)
Worldview 1 Satellite Panchromatic Image (©Maxar)	14 April 2018	50
UAV Orthomosaic	24 July 2018	4
UAV Orthomosaic	29 July 18	4
UAV Orthomosaic	3 August 2018	4
UAV Orthomosaic	30 September 2018	4
Worldview 2 Satellite Panchromatic Image (©Maxar)	5 April 2019	46
Airborne (MACS-Polar) Orthomosaic	13 July 2019	10
Airborne (MACS-Polar) Orthomosaic	23 July 2019	10
Airborne (MACS-Polar) Orthomosaic	30 July 2019	10
UAV Orthomosaic	2 August 2019	4
UAV Orthomosaic	6 August 2019	4
UAV Orthomosaic	10 August 2019	4
UAV Orthomosaic	12 August 2019	4
UAV Orthomosaic	15 August 2019	4
Worldview 2 Satellite Panchromatic Image (©Maxar)	26 September 2019	46
Worldview 2 Satellite Panchromatic Image (©Maxar)	3 April 2020	46

**Table 2.** Summary of remote sensing datasets.(source, date of acquisition and pixel resolution) used in this study.

were georeferenced based on inertially aided multi-frequency, multi-constellation GNSS before export for post-processing to final products. The resolution of orthomosaics is 10 cm.

In 2018, a DJI Phantom 4 UAV was used for all surveys. Flight altitude was 70 m and average speed was 5 m/s. In 2019, a DJI Phantom 4 RTK (Real-Time Kinematic) UAV was used for all surveys and had a flight altitude of 120 m with average speed of 7 m/s. The number of photos taken range between 591 and 726 in 2018 and between 870 and 1000 in 2019 that were post-processed in Pix4 d software to create orthomosaics and digital surface models (DSMs). Absolute horizontal error was on average 7 cm, relative horizontal error was on average 2 cm and average height error was 3 cm. Orthomosaics have a 4 cm pixel resolution and DSMs have a 15 cm pixel resolution.

#### Automatic and manual delineation of bluff edge and blocks

Bluff edges were manually digitized for Worldview and airborne MACS-Polar images. Toppled blocks in front of the bluff face were manually digitized for airborne MACS-Polar and UAV images, but Worldview imagery was too coarse to digitize toppled blocks.

We developed an automatic workflow to delineate the coastal bluff edge using all the UAV derived DSMs that was later manually cleaned to fix errors generated by wave-action at the coast. All post-processing and analysis using the DSMs was conducted in Arcmap Desktop v.10.8.1 (©ESRI). First, a percent rise slope layer was derived from the DSMs. We defined the bluff edge as the point where the break in slope doubles at 100% slope rise. To isolate the bluff edge, we then used the raster calculator to identify all areas below 100% rise in slope. This output raster layer was then converted to a polygon and because the output also contained polygons associated with other features such as blocks, the “Multipart to Singlepart” tool was used to separate all polygons into individual features that can be individually selected. The polygon representing the bluff edge was then selected and exported to create a new layer. This layer was then converted to a polyline and parts (representing edges of the image) were clipped and exported as a new polyline so that only a single line, representing the bluff edge, remained. This polyline was then manually cleaned up using the editor toolbar to correct areas where wave action interfered with the bluff edge delineation and caused errors in bluff edge location (usually driving the bluff edge offshore).

#### Determining erosion rates

Overall rates of coastal erosion were determined using the Digital Shoreline Analysis System v.5.0 (DSAS) ArcGIS Desktop software extension tool<sup>45</sup>. Transect lines were generated every 1 m to measure erosion between each bluff edge timestep. To estimate errors in erosion rate measurements, we calculated the dilution of accuracy<sup>26</sup> for each DSAS run that ranged between 1 cm and 4.7 m. We estimate the average error of erosion (accounting for all DSAS runs) to be  $\pm 13.5$  cm. Sources of error include rms error from image registration, image sources and resolution, and methods for delineating the bluff edge (manual vs. automated methods described in Sect. 3.2).

Transects were visually classified for each DSAS run to determine erosion rates based on erosion process (thermal abrasion or thermal denudation). To determine rates of erosion based on the presence of toppled blocks in front of the bluff edge, toppled blocks were converted to rectangles using the “Minimum Boundary Geometry” tool using the “Envelope Option”. These rectangles were then moved and clipped onto the bluff edge to classify sections of coast as protected or exposed. These clipped bluff edges were also used to classify DSAS transects using the “Select by Location” tool to determine erosion rates along protected or exposed sections of the coast. Note that daily mean erosion rates account for noise and errors within the calculation, but the retreat rates based on erosion mechanism do not as they were visually classified, and therefore the percent transects do not add up to 100.

## Environmental data

Open water season length was determined using a combination of daily satellite data from the NASA Moderate Resolution Imaging Spectroradiometer (MODIS) and the European Space Agency (ESA) Sentinel, Sentinel 1 and 2 imagery (all accessed using <https://www.sentinel-hub.com/explore/eobrowser/>) to determine the ice on and off dates. When gaps were present due to cloudiness or lack of image availability, we took the middle date of the time periods.

Most environmental data was provided by the USGS automatic weather station<sup>37</sup> however precipitation data for 2018 and 2019 was not available, due to faulty sensors. Therefore, hourly precipitation was obtained for Utqiagvik, located 100 km west from Drew Point from the National Centers for Environmental Information (accessed <https://www.ncdc.noaa.gov/>). Ground temperatures collected at the USGS automatic weather station<sup>37</sup> were available at soil depths of 5 cm, 10 cm, 15 cm, 20 cm, 25 cm, 30 cm, 45 cm, 70 cm, 95 cm, and 120 cm. We averaged the temperatures between 5 cm and 30 cm to represent the active layer, and between 45 cm and 120 cm to represent the upper permafrost. SST data was obtained from the NOAA OI SST V2 High Resolution Dataset (accessed <https://psl.noaa.gov/data/gridded/data.noaa.oisst.v2.highres.html>).

To determine storms and storm count, we used the definition from Jones et al.<sup>21</sup> and therefore considered storms to have wind speeds at or exceeding 5 m/s for more than 12 h with less than 6 consecutive hours of lulls and with wind directions between 0° and 90°; and between 240° and 360°. Windrose diagrams were created using WRPLOT View Freeware v.8.0.2. Total wind sums were determined by adding all hourly mean wind speeds for the time period of interest (either sub-seasonal timestep or total annual OWS). Directional wind sums are determined using the same method as total wind sums, except wind speeds between specific direction of interest are summed.

Linear regression and multiple linear regression analysis between erosion amounts and environmental parameters (at both sub-seasonal and annual timescales) was conducted in SigmaPlot v.14 software. Certain transformations (log and removal of outliers) were performed to ensure that each regression output satisfied both normality and constant variance tests. Transformation of log 10 was done for total wind sums and sub-seasonal total, block and denudation erosion as well as for directional wind sum (240° and 90°) and sub-seasonal total erosion. One outlier was removed from the TDD sums and sub-seasonal denudation erosion regression analysis. Regression analysis between sub-seasonal denudation erosion and directional wind sums was not included due to regression outputs not satisfying normality and constant variance tests. For annual regression analysis, 2009 was excluded in runs with directional wind sums and 2017 was excluded in runs with TDD due to data gaps.

## Data availability

How to access external datasets for environmental parameters is described in the methods section. Derived products (i.e. digitized shorelines and toppled permafrost blocks) are available at the Arctic Data Center (ADC) at <https://doi.org/10.18739/A2N873213> (Ward Jones & Jones<sup>46</sup>), and UAV orthomosaics and digital surface models are available at the ADC at <https://doi.org/10.18739/A2HM52M8P> (Ward Jones & Jones<sup>47</sup>). MACS-Polar images are available at PANGEA at <https://doi.org/10.1594/PANGAEA.962561> (Rettelbach et al.<sup>48</sup>). Any questions regarding the datasets and access can be directed to the corresponding author, Melissa Ward Jones (mkwardjones@alaska.edu).

Received: 13 March 2025; Accepted: 28 May 2025

Published online: 05 June 2025

## References

1. Lantuit, H. et al. The Arctic coastal dynamics database: A new classification scheme and statistics on Arctic permafrost coastlines. *Estuaries Coasts*. **35**, 383–400 (2012).
2. Irgang, A. M. et al. Drivers, dynamics and impacts of changing Arctic Coasts. *Nat. Rev. Earth Environ.* **3**, 39–54 (2022).
3. Shabanova, N., Ogorodov, S., Shabanov, P. & Baranskaya, A. Hydrometeorological forcing of Western Russian Arctic coastal dynamics: XX-Century history and current state. *Geogr. Environ. Sustain.* **11**, 113–129 (2018).
4. Jones, B. M. et al. Arctic Report Card 2020: Coastal Permafrost Erosion. (2020).
5. Nielsen, D. M. et al. Increase in Arctic coastal erosion and its sensitivity to warming in the twenty-first century. *Nat. Clim. Change*. **12**, 263–270 (2022).
6. Farquharson, L. M. et al. Temporal and Spatial variability in coastline response to declining sea-ice in Northwest Alaska. *Mar. Geol.* **404**, 71–83 (2018).
7. Ping, C. L. et al. Soil carbon and material fluxes across the eroding Alaska Beaufort sea coastline. *J Geophys. Res. Biogeosciences* **116**, G02004 (2011).
8. Tanski, G. et al. Rapid CO<sub>2</sub> release from eroding permafrost in seawater. *Geophys. Res. Lett.* **46**, 11244–11252 (2019).
9. Nielsen, D. M. et al. Reduced Arctic ocean CO<sub>2</sub> uptake due to coastal permafrost erosion. *Nat. Clim. Change*. **14**, 968–975 (2024).
10. Bristol, E. M. et al. Eroding permafrost coastlines release biodegradable dissolved organic carbon to the Arctic ocean. *J. Geophys. Res. Biogeosciences* **129**, e2024JG008233 (2024).
11. Fritz, M., Vonk, J. E. & Lantuit, H. Collapsing Arctic coastlines. *Nat. Clim. Change*. **7**, 6–7 (2017).
12. Irgang, A. M. et al. Variability in rates of coastal change along the Yukon coast, 1951 to 2015. *J. Geophys. Res. Earth Surf.* **123**, 779–800 (2018).
13. Liew, M. et al. Understanding effects of permafrost degradation and coastal Erosion on civil infrastructure in Arctic coastal villages: A community survey and knowledge Co-Production. *J. Mar. Sci. Eng.* **10**, 422 (2022).
14. Aré, F. E. Thermal abrasion of sea Coasts (Part I). *Polar Geogr. Geol.* **12**, 1–1 (1988).
15. Aré, F. E. Thermal abrasion of sea Coasts (Part II). *Polar Geogr. Geol.* **12**, 87–87 (1988).
16. Günther, F., Overduin, P. P., Sandakov, A. V., Grosse, G. & Grigoriev, M. N. Short- and long-term thermo-erosion of ice-rich permafrost Coasts in the Laptev sea region. *Biogeosciences* **10**, 4297–4318 (2013).
17. Thomas, M. A. et al. Geometric and material variability influences stress States relevant to coastal permafrost bluff failure. *Front Earth Sci* **8**, 143 (2020).
18. Hoque, M. A. & Pollard, W. H. Arctic coastal retreat through block failure. *Can. Geotech. J.* **46**, 1103–1115 (2009).

19. Dallimore, S. R., Wolfe, S. A. & Solomon, S. M. Influence of ground ice and permafrost on coastal evolution, Richards island, Beaufort sea coast, N.W.T. *Can. J. Earth Sci.* **33**, 664–675 (1996).
20. Barnhart, K. R. et al. Modeling erosion of ice-rich permafrost bluffs along the Alaskan Beaufort sea Coast. *J. Geophys. Res. Earth Surf.* **119**, 1155–1179 (2014).
21. Jones, B. M. et al. A decade of remotely sensed observations highlight complex processes linked to coastal permafrost bluff erosion in the Arctic. *Environ. Res. Lett.* **13**, 115001 (2018).
22. Günther, F. et al. Observing Muostakh disappear: permafrost thaw subsidence and erosion of a ground-ice-rich Island in response to Arctic summer warming and sea ice reduction. *Cryosphere* **9**, 151–178 (2015).
23. Berry, H. B., Whalen, D. & Lim, M. Long-term ice-rich permafrost Coast sensitivity to air temperatures and storm influence: lessons from pullen island, Northwest territories, Canada. *Arct. Sci.* **7**, 723–745 (2021).
24. Gibbs, A. E., Erikson, L. H., Jones, B. M., Richmond, B. M. & Engelstad, A. C. Seven decades of coastal change at barter island, alaska: exploring the importance of waves and temperature on Erosion of coastal permafrost bluffs. *Remote Sens.* **13**, 4420 (2021).
25. Solomon, S. M. Spatial and Temporal variability of shoreline change in the Beaufort-Mackenzie region, Northwest territories, Canada. *Geo-Mar. Lett.* **25**, 127–137 (2005).
26. Lantuit, H. & Pollard, W. H. Fifty years of coastal erosion and retrogressive thaw slump activity on herschel island, Southern Beaufort sea, Yukon territory, Canada. *Geomorphology* **95**, 84–102 (2008).
27. Jones, B. M. et al. Increase in the rate and uniformity of coastline erosion in Arctic Alaska. *Geophys. Res. Lett.* **36**, L03503 (2009).
28. Lantuit, H. et al. Coastal erosion dynamics on the permafrost-dominated Bykovsky peninsula, North siberia, 1951–2006. *Polar Res.* **30**, 7341 (2011).
29. Cunliffe, A. M. et al. Rapid retreat of permafrost coastline observed with aerial drone photogrammetry. *Cryosphere* **13**, 1513–1528 (2019).
30. Malenfant, F., Whalen, D., Fraser, P. & van Proosdij, D. Rapid coastal erosion of ice-bonded deposits on Pelly island, southeastern Beaufort sea, Inuvialuit settlement region, Western Canadian Arctic. *Can. J. Earth Sci.* **59**, 961–972 (2022).
31. Tanguy, R., Whalen, D., Prates, G. & Vieira, G. Shoreline change rates and land to sea sediment and soil organic carbon transfer in Eastern Parry Peninsula from 1965 to 2020 (Amundsen gulf, Canada). *Arct. Sci.* **9**, 506–525 (2023).
32. Obu, J. et al. Coastal erosion and mass wasting along the Canadian Beaufort sea based on annual airborne lidar elevation data. *Geomorphology* **293**, 331–346 (2017).
33. Whalen, D. et al. Mechanisms, volumetric assessment, and prognosis for rapid coastal erosion of Tuktoyaktuk island, an important natural barrier for the harbour and community. *Can. J. Earth Sci.* **59**, 945–960 (2022).
34. Smith, S. et al. Thermal state of permafrost in North america: a contribution to the international Polar year. *Permafro. Periglac. Process.* **21**, 117–135 (2010).
35. Kanevskiy, M. et al. Ground ice in the upper permafrost of the Beaufort sea Coast of Alaska. *Cold Reg. Sci. Technol.* **85**, 56–70 (2013).
36. Bristol, E. M. et al. Geochemistry of coastal permafrost and Erosion-Driven organic matter fluxes to the Beaufort sea near drew point, Alaska. *Front Earth Sci* **8**, 598933 (2021).
37. Urban, F. E. & Clow, G. D. *DOI/GTN-P Climate and Active-Layer Data Acquired in the National Petroleum Reserve-Alaska and the Arctic National Wildlife Refuge, 1998–2019*. (2021). <https://doi.org/10.3133/ds1092>
38. Overeem, I. et al. Sea ice loss enhances wave action at the Arctic Coast. *Geophys. Res. Lett.* **38**, 1777–1799 (2011).
39. Barnhart, K. R., Overeem, I. & Anderson, R. S. The effect of changing sea ice on the physical vulnerability of Arctic Coasts. *Cryosphere* **8**, 1777–1799 (2014).
40. Frederick, J., Mota, A., Tezaur, I. & Bull, D. A thermo-mechanical terrestrial model of Arctic coastal erosion. *J. Comput. Appl. Math.* **397**, 113533 (2021).
41. Bayat, E. et al. The Arctic coastal Erosion model: overview, developments, and calibration at drew point, Alaska. *Preprint source, ESS Open Archive* (2025).
42. Bryant, M. B. et al. Multiple modes of shoreline change along the Alaskan Beaufort Sea observed using ICESat-2 altimetry and satellite imagery. *The Cryosphere* **19**, 1825–1847 (2025).
43. Tsai, Y. L. S. Monitoring Arctic permafrost coastal erosion dynamics using a multidecadal cross-mission SAR dataset along an Alaskan Beaufort sea coastline. *Sci. Total Environ.* **917**, 170389 (2024).
44. Rettelbach, T. et al. Very high resolution aerial image orthomosaics, point clouds, and elevation datasets of select permafrost landscapes in Alaska and Northwestern Canada. *Earth Syst. Sci. Data.* **16**, 5767–5798 (2024).
45. Himmelstoss, E. A., Henderson, R. E., Kratzmann, M. G. & Farris, A. S. Digital shoreline analysis system (DSAS) version 5.0 user guide. *Open-File Rep.* <https://doi.org/10.3133/ofr20181179> (2018). <https://pubs.usgs.gov/publication/ofr20181179>
46. Ward Jones, M. & Jones, B. Derived coastlines and toppled permafrost blocks at drew point, beaufort, sea coast, alaska, 2018 and 2019. *Arct. Data Cent.* <https://doi.org/10.18739/A2N873213> (2025).
47. Ward Jones, M. & Jones, B. Orthomosaic images and digital surface models at drew point, Beaufort sea, coast, alaska, 2018 and 2019. *Arct. Data Cent.* <https://doi.org/10.18739/A2HM52M8P> (2025).
48. Rettelbach, T. et al. Super-high-resolution aerial imagery, digital surface models and 3D point clouds of Drew Point, Alaska. <https://doi.pangaea.de/> (2024). <https://doi.org/10.1594/PANGAEA.962561>

## Acknowledgements

Funding provided for this research includes the US National Science Foundation – awards OISE-1927553, OIA-1929170, RISE-2318375, and OPP-2336164. This work was additionally supported by the Sandia National Laboratories Laboratory Directed Research & Development Program; Sandia National Laboratories is a multi-mission laboratory managed and operated by National Technology and Engineering Solutions of Sandia, LLC., a wholly owned subsidiary of Honeywell International, Inc., for the U.S. Department of Energy's National Nuclear Security Administration under grant ~DE-NA-0003525. Additional support was provided by Earth Observation for Permafrost dominated Arctic Coasts (EOC4PAC) project funded by the European Space Agency (4000134425/21/I-NB) and through a Broad Agency Announcement award from ERDC-CRREL, PE 0603119 A. Funding for the Polar-6 airborne operations was provided through Alfred Wegener Institute base funds for the ThawTrend-Air 2019 campaign. We thank the three anonymous reviewers for their comments and suggestions in improving the manuscript.

## Author contributions

M.W.J. conducted the analysis, wrote the first draft of the manuscript, created the figures, contributed to conception, revision and editing of the manuscript. B.J. collected and post-processed all UAV data, contributed to the analysis, contributed to conception, revision and editing of the manuscript. I.N., M.G., and G.G., collected and post-processed the MACS-Polar imagery, contributed to conception, revision and editing of the manuscript. A.B. and D.B. contributed to the conception, revision, and editing of the manuscript.

## Declarations

### Competing interests

The authors declare no competing interests.

### Additional information

**Correspondence** and requests for materials should be addressed to M.K.W.J.

**Reprints and permissions information** is available at [www.nature.com/reprints](http://www.nature.com/reprints).

**Publisher's note** Springer Nature remains neutral with regard to jurisdictional claims in published maps and institutional affiliations.

**Open Access** This article is licensed under a Creative Commons Attribution-NonCommercial-NoDerivatives 4.0 International License, which permits any non-commercial use, sharing, distribution and reproduction in any medium or format, as long as you give appropriate credit to the original author(s) and the source, provide a link to the Creative Commons licence, and indicate if you modified the licensed material. You do not have permission under this licence to share adapted material derived from this article or parts of it. The images or other third party material in this article are included in the article's Creative Commons licence, unless indicated otherwise in a credit line to the material. If material is not included in the article's Creative Commons licence and your intended use is not permitted by statutory regulation or exceeds the permitted use, you will need to obtain permission directly from the copyright holder. To view a copy of this licence, visit <http://creativecommons.org/licenses/by-nc-nd/4.0/>.

© The Author(s) 2025